Materials Science & Engineering C 124 (2021) 111937

Contents lists available at ScienceDirect

Materials Science & Engineering C

journal homepage: www.elsevier.com/locate/msec

Barium yttrium fluoride based upconversion nanoparticles as dual mode image contrast agents

Padmaja Parameswaran Nampi [a,b,c,*,1], Alexander Vakurov [b], Hema Viswambharan [c], Jürgen E. Schneider [c], Rik Brydson [a,1], Paul A. Millner [b], Sikha Saha [c,1], Gin Jose [a,1]

[a] School of Chemical and Process Engineering, Faculty of Engineering and Physical Sciences, University of Leeds, Leeds LS2 9JT, United Kingdom
[b] School of Biomedical Sciences, Faculty of Biological, Sciences, University of Leeds, Leeds LS2 9JT, United Kingdom
[c] Leeds Institute of Cardiovascular and Metabolic Medicine (LICAMM), Faculty of Medicine and Health, University of Leeds, Leeds LS2 9JT, United Kingdom

ARTICLE INFO

Keywords:
Nanomaterials
Luminescence upconversion
Upconversion nanoparticles
CT contrast

ABSTRACT

Dual labeled contrast agents could provide better complementary information for bioimaging than available solely from a single modality. In this paper we investigate the suitability of Yb^{3+} and Er^{3+}-doped $BaYF_5$ upconversion nanoparticles (UCNPs) as both optical and X-ray micro computed tomography (μCT) contrast agents. Stable, aqueous UCNP dispersions were synthesised using a hydrothermal method with the addition of polyethyleneimine (PEI). UCNPs were single crystal and had a truncated cuboidal morphology, with average particle size of 47 ± 9 nm from transmission electron microscopy which was further used to characterize the structure and composition in detail. A zeta potential value of +51 mV was measured for the aqueous nanoparticle dispersions which is beneficial for cell permeability. The outer hydrated PEI layer is also advantageous for the attachment of proteins for targeted delivery in biological systems. The prepared UCNPs were proven to be non-toxic to endothelial cells up to a concentration of 3.5 mg/mL, when assessed using an MTT assay. The particles showed intense green upconversion photoluminescence when excited at a wavelength of 976 nm using a diode laser. Quantitative X-ray μCT contrast imaging confirmed the potential of these UCNPs as X-ray contrast agents and confirming their dual modality for bioimaging.

1. Introduction

Upconversion (UC) is a process that converts two or more lower-energy photons in the near-infrared wavelengths into one higher energy photon in the visible or ultraviolet (UV) wavelengths [1]. Nanoparticles doped with lanthanide ions that can produce efficient upconversion are known as upconversion nanoparticles (UCNPs) and have been proven to be useful as fluorescent labels for biomedical imaging [1–5]. In a biological medium, UCNPs offer advantages such as higher penetration depth of infrared excitation radiation [2–7], excellent photostability and the absence of autofluorescence in comparison to fluorescent dyes, semiconductor quantum dots or down-conversion nanophosphors [8,9]. The long lifetime and ladder-like $4f^n$ energy levels of trivalent lanthanide ions can produce higher energy anti-Stokes luminescence *via* incorporation into low phonon energy (<500 cm^{-1} for fluorides) inorganic host nanocrystals. To be suitable for bioimaging or sensing, the nanocrystalline material for lanthanide ion doping should be transparent in the wavelength range of interest, should have a high optical damage threshold and be chemically stable. Fluoride-based host materials such as LaF_3 and $NaYF_4$ have been the most common materials of choice for effective upconversion as they possess all these characteristics [7–13]. There have been some studies on fluorides such as MF_2 and MF_2-LnF_3 (where M represents a group II element) solid solutions [14–17]. The lanthanide ion-doped barium yttrium fluoride system has also been proposed as a host material due to the structural as well as optical properties [14,18–20]; it is reported that bulk $BaYF_5$ doped with Er^{3+} can present approximately eight times the UC emission than that of Er^{3+}-doped LaF_3 nanocrystals [21]. Glass ceramics containing Er^{3+}-doped $BaYF_5$ nanocrystals have shown 13 times brighter UC emission than correspondingly doped LaF_3 nanocrystals [22]. Syntheses of lanthanide-doped $BaYF_5$ nanocrystals have been carried out by co-decomposition in organic solvents under inert gas atmosphere and high temperature [18–23]. Most of these methods produce hydrophobic nanoparticles which need further surface modification for biological

* Corresponding author.
E-mail address: p.nampi@leeds.ac.uk (P.P. Nampi).
[1] Associated with Bragg Centre for Materials Research, University of Leeds.

https://doi.org/10.1016/j.msec.2021.111937
Received 5 March 2020; Received in revised form 11 November 2020; Accepted 31 January 2021
Available online 6 February 2021
0928-4931/© 2021 The Authors. Published by Elsevier B.V. This is an open access article under the CC BY license (http://creativecommons.org/licenses/by/4.0/).

applications. The synthesis of tetragonal $BaYF_5$ nanocrystals using EDTA as a chelating agent produced red emitting particles in multiple organic solvents with various size ranges depending on the pH as well as dopant concentrations, which were rendered soluble in water by a general PAA exchange procedure [24].

Apart from high UC emission, the barium fluoride system is also reported to show remarkable X-ray contrast [25] due to the high atomic number of Ba, as compared to Na, resulting in a K-edge energy of 37 keV. Hence, the $BaYF_5/Yb^{3+}/Er^{3+}$ system presents significant opportunities for dual modal imaging. Although larger particles will have higher photoluminescence, they are reported to be more susceptible to aggregation so limiting their penetration into cells and making them less suitable for biological imaging applications [26]. Moreover, spectroscopic investigation has revealed that upconversion luminescence intensity is dependent on particle morphology, size, and crystallinity [27]. Hence developing particles of the appropriate size for *in vitro* and *in vivo* imaging of cells with optimum photoluminescence efficiency is of significant interest.

Recent reviews have reported important advances in NIR lanthanide-based UC materials and their biomedical application [28–30]. However, there are few studies of the facile synthesis of aqueous-based UC systems, their complete structural characterisation and correlation with properties, as well as the assessment of their suitability for advanced application. Hence in the present work, we have modified the method to synthesise, and characterised the water dispersible $BaYF_5/Yb^{3+}/Er^{3+}$ nanoparticles coated with polyethyleneimine (PEI) for their use in bio-imaging. The method reported here does not use organic solvents such as cyclohexane or toluene, and the direct dispersion of particles in water allows elimination of an additional hydrophilisation step. Detailed structural characterisation is another novelty of the work which is useful for advanced applications of these UCNPs in optical and X-ray imaging (dual mode) applications, confirmed *via* UC spectroscopy and μCT measurements. The non-toxic effects of these particles have been established *via* testing on endothelial cells, which demonstrates the suitability of the particles for use in biological applications.

2. Experimental

2.1. Nanoparticle synthesis

Branched polyethyleneimine [PEI, Aldrich MW 25,000] and all other reagents including yttrium nitrate hexahydrate $Y(NO_3)_3{\cdot}6H_2O$ (99.9%), ytterbium nitrate pentahydrate $Yb(NO_3)_3{\cdot}5H_2O$ (99.9%), erbium nitrate pentahydrate $Er(NO_3)_3{\cdot}5H_2O$ (99.9%), ammonium fluoride NH_4F (99.5%) and barium nitrate $Ba(NO_3)_2$ (99.5%), were purchased from Sigma Aldrich. All chemicals were of analytical grade and were used without further purification. The final washing of the precipitate and dispersion of the nanoparticles were done using ultrapure water with a conductivity of 0.05 μS/cm, corresponding to a resistivity of 18 megaohm·cm (MΩ·cm).

A modified version of the experimental method adopted by Zhang et al. [31] was used to prepare $BaYF_5$ nanoparticles doped with Yb^{3+}/Er^{3+} using PEI and water as the solvent. The doping ratio was chosen to be $BaY_{0.78}Yb_{0.2}Er_{0.02}F_5$ based on our previous studies of the $NaYF_4/Yb^{3+}/Er^{3+}$ system [32]. As the main objective of this current investigation was to test the suitability of these Ba-based UCNPs for dual mode imaging, we have not yet further optimised the doping ratio for this Ba-based system, which will be the subject of a future study.

In the first step, 1.6 g of PEI was dissolved in 15 mL of deionised water keeping the temperature at 50 °C. A second solution was prepared using 3.12 mmol of $Y(NO_3)_3{\cdot}6H_2O$, 0.8 mmol of $Yb(NO_3)_3{\cdot}5H_2O$, 0.08 mmol of $Er(NO_3)_3{\cdot}5H_2O$ and 4 mmol of $Ba(NO_3)_2$ in 60 mL of deionised water. To this solution, the PEI solution was added dropwise followed by an ammonium fluoride solution (100 mmol of NH_4F dissolved in 30 mL of deionised water) and this was stirred for 30 min to obtain a uniform homogenous mixture. The resultant solution yielded nanoparticles of the composition $BaY_{0.78}Yb_{0.2}Er_{0.02}F_5$. The pH of the solution was measured to be around 7.5. The solution was then transferred into a Teflon container and placed within a Parr pressure vessel, and heated at a temperature of 180 °C for 24 h in an oven. The resultant solution was then allowed to cool down to room temperature. The contents including the nanoparticulate precipitate in the cooled solution were then washed 3–4 times with ultrapure water by repeated ultracentrifugation at 80,000*g* for 30 min using a Beckman Avanti J20XP high speed centrifuge. The nanoparticle pellet thus obtained was re-dispersed in MilliQ water by sonication using an ultrasonic probe for a maximum of 2 min (Bandekin GM2070 with 100% power; cycle 0.7 s). The concentration of the suspension was determined to be 35 mg/mL. It was diluted 10 times and ultrasonicated before measuring the UC fluorescence and diluted as per the requirements for other measurements.

2.2. X-ray diffraction (XRD)

X-ray diffraction (XRD) measurements were made with a PANalytical X'Pert Pro Multipurpose Diffractometer at a scanning rate of 4°/min in the 2θ range from 20° to 80°, with Cu Kα radiation (λ = 1.5406 A°). An accelerating voltage and current of 40 kV and 40 mA respectively were used for measurement.

2.3. Transmission electron microscopy (TEM)

TEM samples were prepared by placing a diluted drop of UCNPs onto a holey carbon-coated copper TEM grid. TEM measurements were performed using a FEI Titan Themis 300 G2 FEG S/TEM operated at 300 kV and equipped with a Gatan OneView 16 Megapixel CMOS digital camera and Super-X EDX system with a windowless 4-detector design. Selected area electron diffraction (SAED) and lattice spacings in the images were analysed to confirm the crystallinity of the UCNPs. EDX analysis was used to obtain the approximate atomic ratios of the elements present in the UCNPs. The size-distribution histogram of nanoparticles was determined by image analysis (ImageJ software) of low magnification TEM images. High angle annular dark field (HAADF) scanning TEM (STEM) imaging and EDX mapping were carried out with a 1000 nA probe current and 23 μs dwell time with a specimen pixel size of 4 nm. High signal to noise ratio atomic resolution STEM HAADF images were recorded with a HAADF inner detector angle of 43.5 mrad and obtained by stacking of up to 93 frames; the accumulated electron dose being 8×10^4 electrons/$Å^2$.

2.4. Dynamic light scattering (DLS)

A Malvern Zetasizer Nano ZS system (Malvern, UK) was used to determine the average hydrodynamic diameter and zeta potential of the nanoparticle suspension at a concentration of 3.5 mg/mL.

2.5. Luminescence measurements

The measurement of luminescence spectra and the corresponding decay curves of the nanoparticle suspensions were undertaken in a Spectrofluorimeter (Edinburgh Instruments, UK). The samples were excited using a focused 976 nm continuous wave (CW) laser with an approximate power density at focus of 162 kW/m^2. The UC photoluminescence spectrum was measured in the wavelength range 400–800 nm. The decay of the UC photoluminescence were measured by modulating the laser at 100 Hz and the decay time obtained by linear fitting of the logarithmic intensity data.

2.6. Fluorescence microscopy

Fluorescence images of the particles were captured using a Zeiss Imager Z1 AX10 Apotome Microscope attached with a 976 nm CW diode laser (BL976-SA300, Thorlabs).

2.7. In vitro cytotoxicity evaluation

In vitro cell toxicity studies of UCNPs was performed on human umbilical vein endothelial cells (HUVECs) and assessed using the 3-(4,5-dimethylthiazol-2yl)-2,5-diphenyltetrazolium bromide (MTT) (Sigma Aldrich) assay. Briefly, 10^4 HUVECs were grown overnight in a 96-well plate. The growth medium was prepared using Promocell Endothelial Cell Growth Medium supplemented with Promocell Endothelial cell supplements and 10% (v/v) foetal calf serum. Doses of nanoparticles, ranging from 0.3 μg/mL to 3.5 mg/mL in growth media, were added and incubated for a period of 24 h. The MTT assay was carried out the next day by adding 50 μL of 5 μg/mL MTT to each well. After the addition of MTT, the plate was incubated for a period of 3 h, until the purple product was formed. The control corresponds to cells without particles. These purple crystals were dissolved using 300 μL/well of isopropanol and the plate was read using 576 nm illumination using a Bio-Rad (Model-680) microplate reader.

2.8. Micro computed tomography (μCT) contrast

X-ray micro computed tomography (μCT) images of the samples were taken in a SkyScan 1176 μCT Scanner, using a source voltage of 65 kV, a source current of 380 (μA), and a 1 mm Al filter. The image reconstructions were performed using NRecon software with a smoothing parameter of 5, a ring artefact correction of 11 and a beam hardening correction of 30%. Inside each sample, equally sized round volume of interests (VOIs) were drawn and reconstructed. Image analysis was executed with CTAn, with values calibrated to water.

3. Results and discussion

3.1. X-ray diffraction measurements

The X-ray diffraction pattern of the UCNP sample prepared in this research is presented in Fig. 1. The XRD data was found to agree well with ICSD Reference: 169849, which corresponds to sample with a cubic structure [33]. The results are also comparable with the studies of Liu et al. for a similar nanoparticle system where the authors compared the pattern to cubic $BaCeF_5$ (JCPDS Reference: space group-$Fm\bar{3}m$ 43-0394) [19,25]. Residual peaks at 2θ equal to 43° and 49° in Fig. 1 may result from traces of BaF_2 in the compound phase [34].

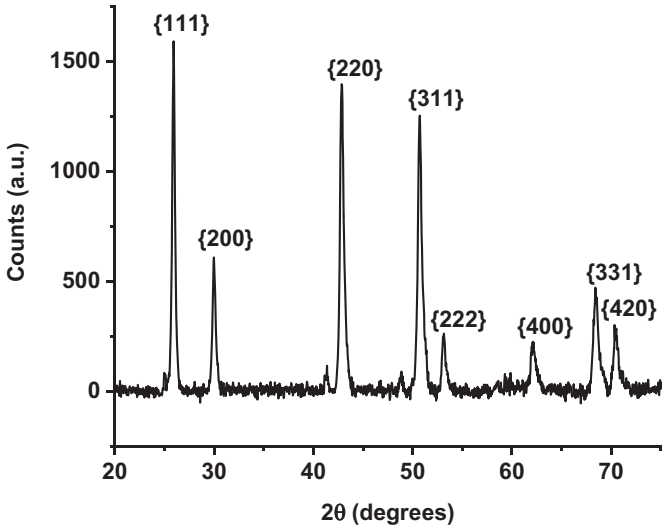

Fig. 1. XRD pattern of $BaYF_5/Yb^{3+}/Er^{3+}$ UCNP sample.

BaF_2 is matched with the ICSD Reference: 41649. It is reported that cubic BaF_2 acts as a structural director for the formation of cubic $BaYF_5$ nanocrystals [19]. The presence of these additional XRD peaks may also possibly correspond to very mild traces of the tetragonal $BaYF_5$ phase [33]. However, this latter explanation was ruled out for the nanoparticles reported here as these XRD peaks do not correspond to JCPDS Reference: 46-0039 corresponding to the tetragonal phase and were also not observed in the TEM analysis presented below. More detailed XRD patterns showing the fitted calculated curve, *via* the Rietveld method and the stick models corresponding to cubic $BaYF_5$, cubic $BaCeF_5$, BaF_2 and tetragonal $BaYF_5$ compared to the original measured XRD of the sample is presented in Fig. S1. The refinement shows a weighted profile R-factor (R_{wp}) value of 0.0049, consisting of 98.70 wt% $BaYF_5$ and 1.30 wt% BaF_2. The calculated lattice parameter of the UCNP sample is 0.5962 ± 0.0016 nm. From a Williamson Hall analysis (Fig. S2) using the {111}, {200}, {220}, {311} XRD peaks, the average crystallite size was calculated to be 36.5 ± 6.4 nm with a lattice strain $0.27 \pm 0.07\%$.

3.2. High resolution transmission electron microscopy

High resolution, phase contrast conventional TEM (CTEM) images and selected area electron diffraction (SAED) patterns of the synthesised nanoparticles are shown in Fig. 2. Fig. 2a is a CTEM image of particles recorded at 45,000× magnification suggesting the particles have a cuboidal, truncated cuboidal and truncated octahedral morphology and, owing to the presence of diffraction contrast, are crystalline.

The particle size distribution, obtained from a larger number of particles (*ca.* 100) is shown in Fig. 2b. Particles were distributed over the size range of 20–75 nm with a mean size of 47 ± 9 nm in good agreement with the crystallite size derived using XRD. The interplanar spacings (d_{hkl}) obtained from the selected area electron diffraction (SAED) pattern (Fig. 2c) were: $d_{111} = 0.347 \pm 0.014$ nm, $d_{200} = 0.304 \pm 0.012$ nm, $d_{220} = 0.214 \pm 0.008$ nm and $d_{311} = 0.182 \pm 007$ nm corresponding to a cubic lattice [19] with a lattice constant, a calculated to be 0.604 ± 0.021 nm. A comparison of the d spacings and lattice parameter calculated from TEM and XRD is presented in Supporting Information as Table S1. The lattice parameters derived from XRD ($a = 0.5962 \pm 0.0016$ nm) and TEM ($a = 0.604 \pm 0.021$ nm) agree within experimental error. Fig. 2d shows a higher magnification image (570,000×) of a single particle showing a truncated cuboidal shape while Fig. 2e corresponds to the fast Fourier transformed (FFT) image of the area marked in Fig. 2d which confirmed that the crystal lattice is face centered cubic [35]. The spots in the FFT are labeled with their {hkl} notation and it is clear from a comparison of Fig. 2d and e that the surface normals and hence large surface facets are predominantly {111} type with additional {100} type facets indicating strictly a truncated octahedral morphology. Fig. 3a is a high-resolution CTEM image revealing lattice fringes recorded from the particle shown in Fig. 2d; lattice fringes extend across the whole particle indicating that it is single crystal in nature. A Fourier filtered image of the lattice is shown in Fig. 3b and the intensity profile in Fig. 3c indicates an average d spacing of 0.345 nm, close to the {111} lattice spacing.

EDX spectra of the nanoparticles (Fig. S3) showed the presence of the main elements in atomic ratios, very comparable to the expected theoretical composition derived from the synthesis procedure. The average atomic% of the elements determined from EDX spectra from four different areas, each containing a cluster of nanoparticles, together with

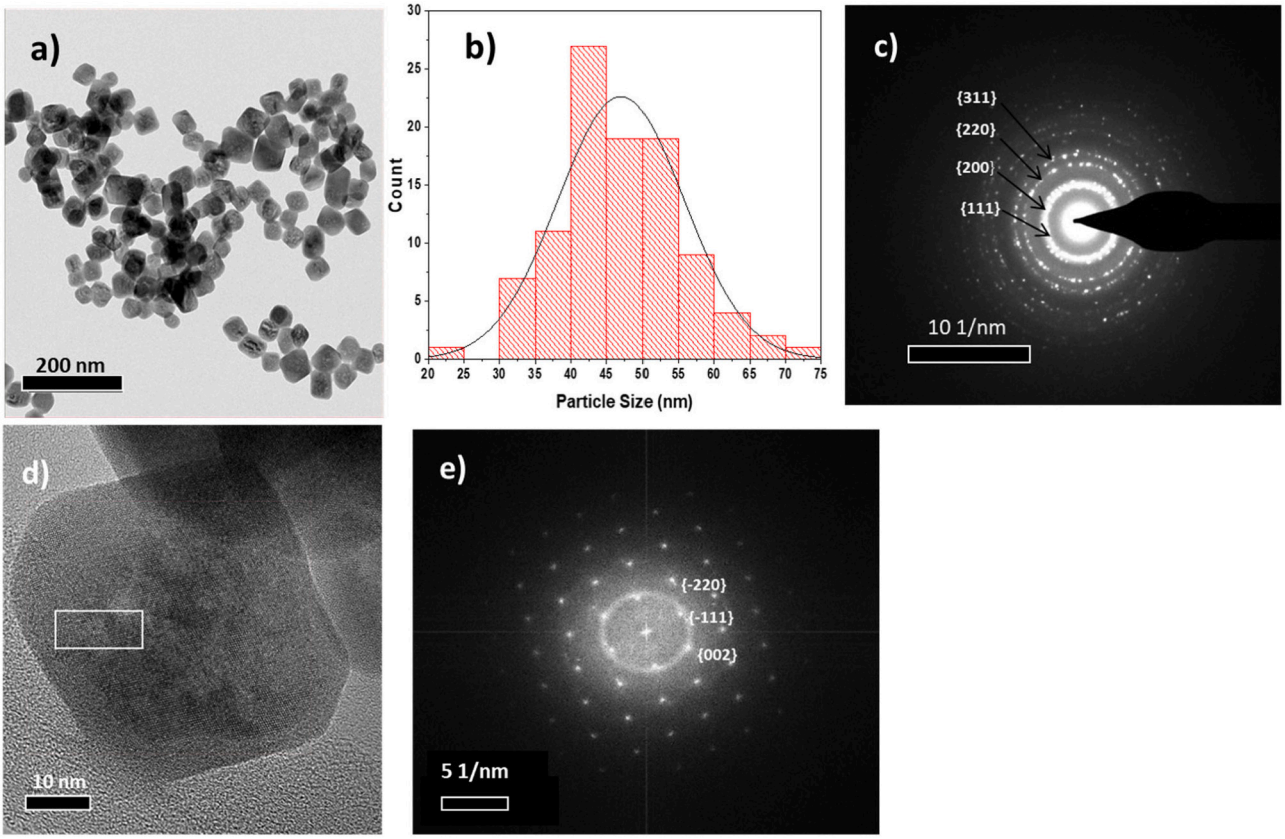

Fig. 2. a) CTEM image of $BaYF_5/Yb^{3+}/Er^{3+}$ UCNPs showing the particle morphology. b) The particle size distribution elucidated from approximately 100 particles. c) SAED pattern from a group of particles indicating a cubic lattice structure viewed down ⟨110⟩ direction. d) Single particle morphology showing a cuboidal shape. e) FFT of the area inside the white box indicated in d showing the face centered cubic lattice viewed down the <110> direction.

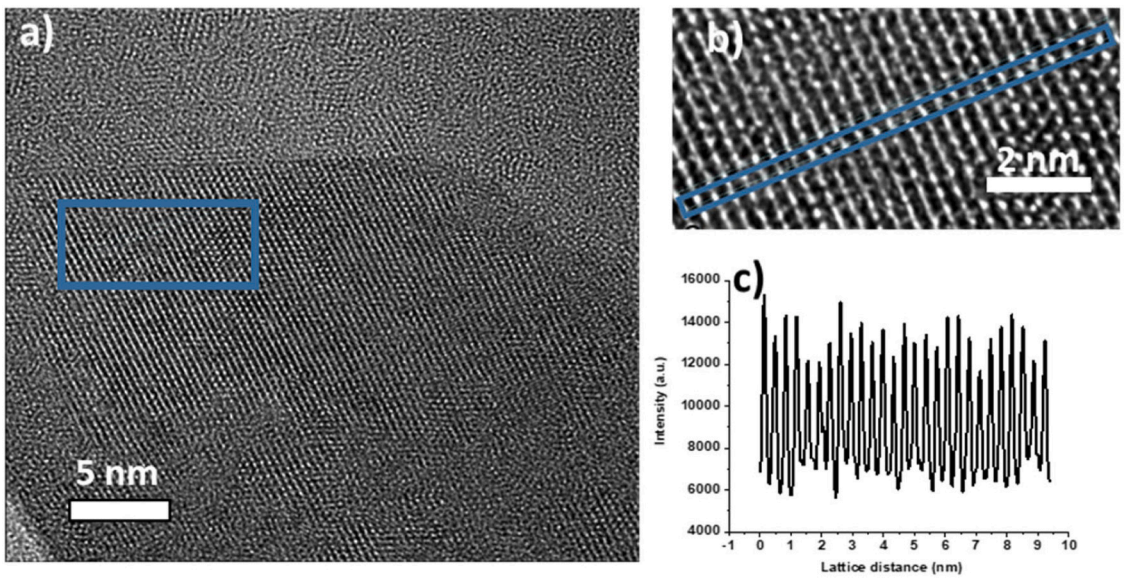

Fig. 3. a) High resolution CTEM image of a $BaYF_5/Yb^{3+}/Er^{3+}$ UCNP. b) Fourier filtered image from the boxed area indicated in a indicates the particle is being viewed down the <110> direction. c) Intensity profile of fringes along the line in b showing a lattice spacing of 0.345 nm corresponding to the {111} planes.

the calculated theoretical atomic% values are presented in Table 1. The experimental values indicate that the sample shows only relatively minor variations in homogeneity and are close to the desired composition.

In order to assess further the variation in elemental composition between particles, high angle annular dark field (HAADF) STEM imaging and STEM/EDX mapping of the various elements were recorded. Fig. 4a shows a STEM HAADF image of a group of nanoparticles and

Table 1
Comparison of theoretical atomic % and atomic % obtained from EDX spectra recorded from four different $BaYF_5/Yb^{3+}/Er^{3+}$ UCNP areas.

Elements	Calculated atomic % based on desired composition $BaY_{0.78}Yb_{0.2}Er_{0.02}F_5$	Average atomic % determined from four EDX spectra obtained from different areas
Ba	14.3	21.9 ± 2.4
Y	11.1	9.2 ± 1.2
Yb	2.9	2.1 ± 0.3
Er	0.3	0.5 ± 0.3
F	71.4	66.2 ± 2.9

STEM/EDX elemental mapping (Fig. 4b–f) qualitatively indicates the presence of all major elements evenly distributed amongst the particles.

Fig. 5a is a magnified HAADF STEM image showing relatively even Z-contrast, indicative of compositional homogeneity within and between particles (except where particle overlap is apparent). A STEM/EDX line scan across an aggregate of three particles is presented in Fig. 5b (HAADF image and line scan position) and 5c (EDX intensity profiles). Again the results show an absence of intraparticle segregation and a reasonably homogeneous distribution of elements. Note any variation in the fluorine signal (and overall composition in Table 1) may be due to its beam sensitivity relative to the other elements present.

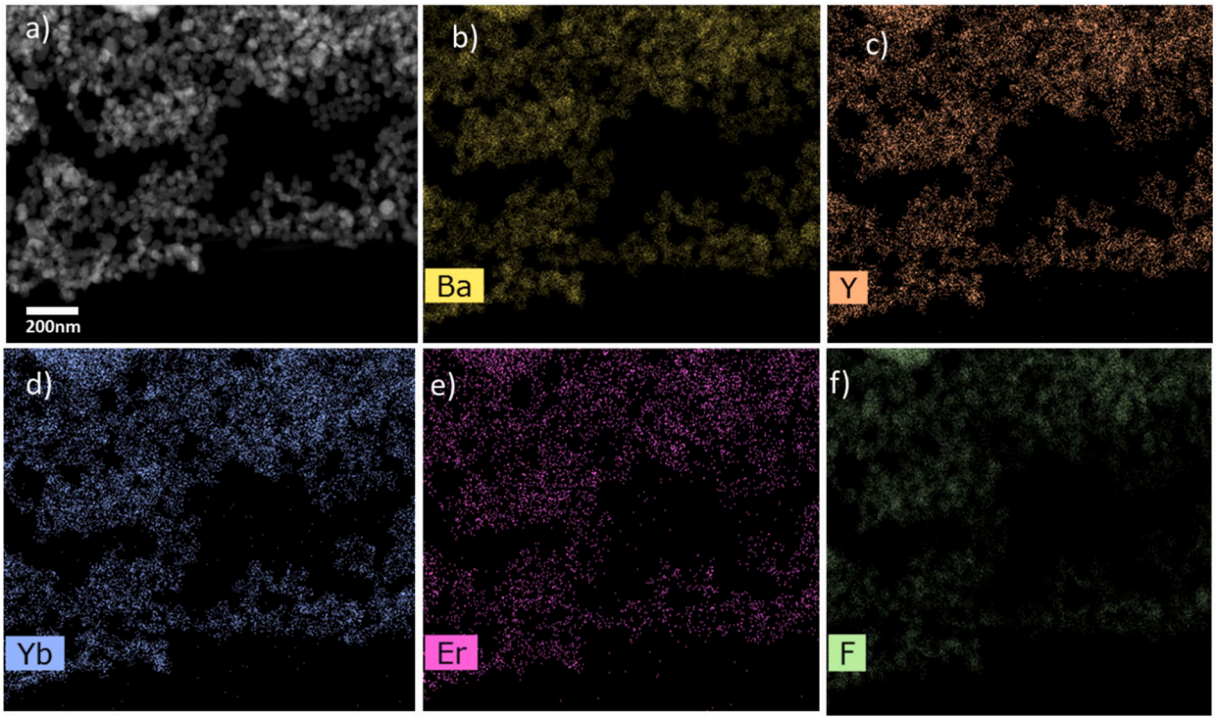

Fig. 4. a) STEM HAADF image of the $BaYF_5/Yb^{3+}/Er^{3+}$ UCNPs. b–f) shows the STEM/EDX maps for the various major elements present.

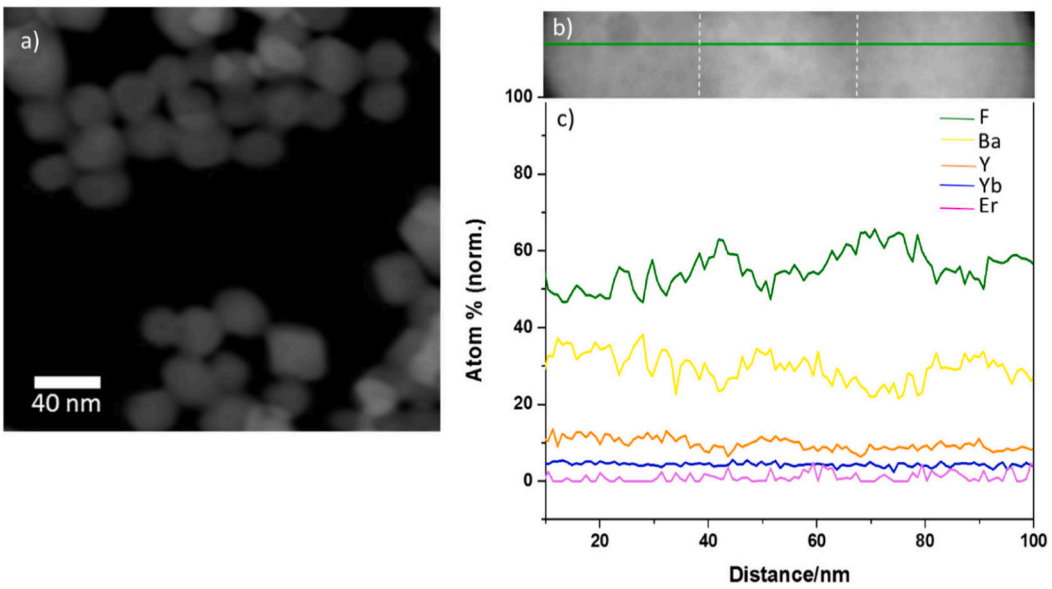

Fig. 5. a) Higher magnification STEM HAADF image of $BaYF_5/Yb^{3+}/Er^{3+}$ UCNPs. b) Line scan position indicated across an aggregate of 3 particles and c) STEM/EDX line scans along the line indicated in b.

3.3. Particle size distribution and zeta potential from dynamic light scattering (DLS)

The particle size distribution of UCNPs in aqueous solution and their zeta potential was measured using DLS and the results are reported in Fig. 6. From Fig. 6a we can see that relatively monodispersed particles with mean hydrodynamic particle diameter of around 90 nm dominate the particle size distribution. This is higher than the average size obtained from TEM (Fig. 2b) and is consistent with hydrodynamic diameters generally obtained in DLS measurement, whereby the hydrodynamic diameter includes the contribution of the surfactant coating [36]. PEI-UCNP particles showed long-term stability in an aqueous environment without any noticeable aggregation. The maximum zeta potential value of +51 mV for the particles obtained from the zetasizer analysis measurement is presented in Fig. 6b. It suggests that PEI-UCNPs had cationic surfaces attributed to the protonated amino groups of the PEI at neutral pH which act as a hydrophilic head. This repulsion between cationic particles results in a highly stable dispersion which showed excellent long-term stability which was assessed by DLS measurement of the aqueous dispersion after 6 months and revealed no noticeable change in the particle hydrodynamic size distribution and no observable sedimentation of the particles. Aggregation does occur at higher pH when the nanoparticles are deprotonated. The pH of our synthesised aqueous suspension is found to be 7.5, where the particles are well dispersed. The stability of the particles in hydrophilic conditions makes these particles attractive for biological applications. The positive zeta potential is also advantageous for better cell membrane permeability, relative to negatively charged particles [37]. Thus, overall the high positive zeta potential value of the UCNPs is beneficial for tissue and cellular imaging.

3.4. Cytotoxicity analysis

Cytotoxicity is an important concern where the application of nanoparticles in biological systems is considered. Hence, the toxicity of the PEI-coated nanoparticles towards endothelial cells was evaluated using the MTT assay. Fig. 7 shows the cell viability data, which is a measure of the cytotoxicity of the sample. The data indicated no toxicity on endothelial cells with UCNP concentration ranging from 0.3 μg/mL to 3.5 mg/mL, compared to control (cells without particles). Exposing the cells to the UCNPs for 24 h resulted in an average cell viability of 90–100%.

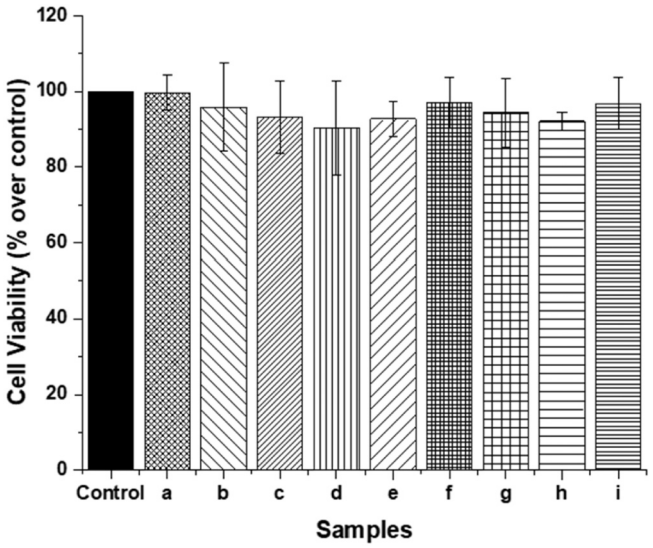

Fig. 7. MTT assay of the UCNPs showing practically no cytotoxicity compared to the control: a) 0.3 μg/mL b) 3 μg/mL c) 30 μg/mL d) 300 μg/mL e) 500 μg/mL f) 700 μg/mL g) 1 mg/mL h) 3 mg/mL and i) 3.5 mg/mL.

3.5. Photoluminescence and in vitro micro computed tomography (μCT)

Fig. 8a shows a photograph of the as prepared colloidal suspension of the nanoparticles at a concentration of 35 mg/mL while Fig. 8b shows their green UC photoluminescence under diode laser illumination at a wavelength of 976 nm. The luminescence emission spectrum of the UCNP suspension is illustrated in Fig. 8c and shows an intense doublet for green emission as compared to red. The emission bands in the range 510 nm to 530 nm and between 530 and 570 nm corresponding to the $^2H_{11/2} \rightarrow {}^4I_{15/2}$ and $^4S_{3/2} \rightarrow {}^4I_{15/2}$ transitions of Er^{3+} ions contribute to the green emission intensity. The relatively less intense doublet peak in the red wavelength region (635–694 nm) is due to the $^4F_{9/2} \rightarrow {}^4I_{15/2}$ transition [11]. The lineshape of the observed UC spectrum differ from previously reported research in these type of nanoparticles [38,39], and in this research we also report the lifetimes of both green and red emissions. The combination of both red and green emission under 976 nm NIR wavelength excitation appeared more greenish to the eye/camera as shown in Fig. 8b. Owing to their higher absorption cross-

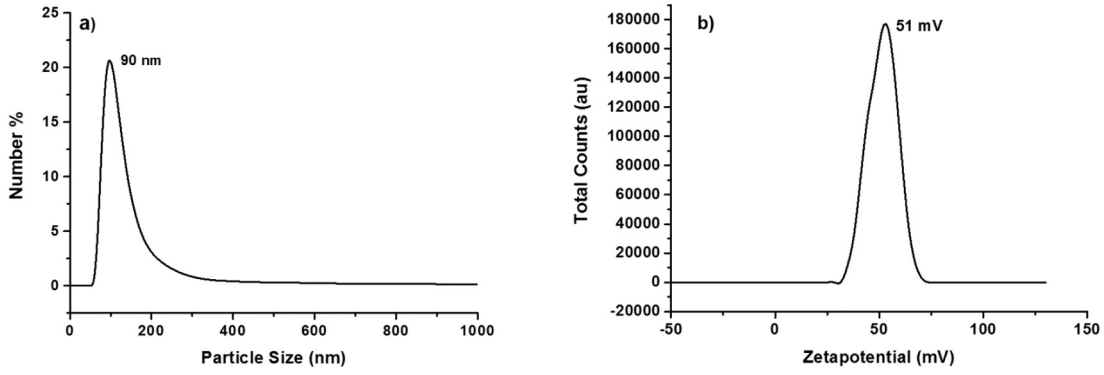

Fig. 6. a) DLS hydrodynamic particle size distribution and b) zeta potential values of the $BaYF_5/Yb^{3+}/Er^{3+}$ UCNP dispersion (concentration of 3.5 mg/mL).

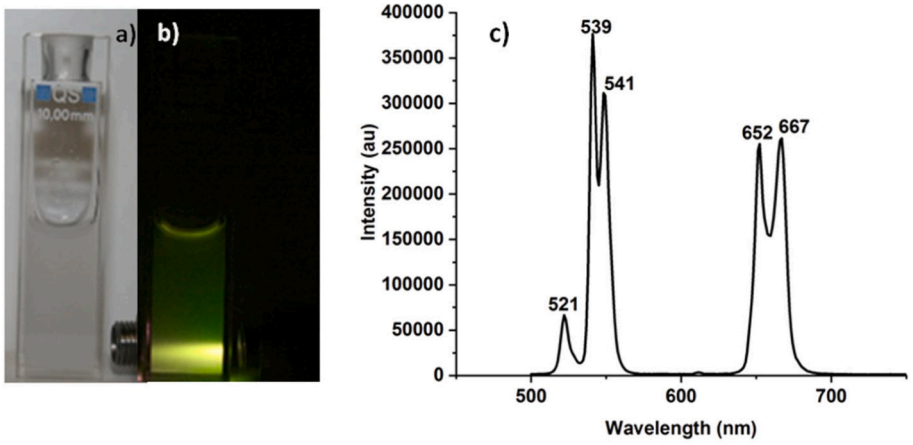

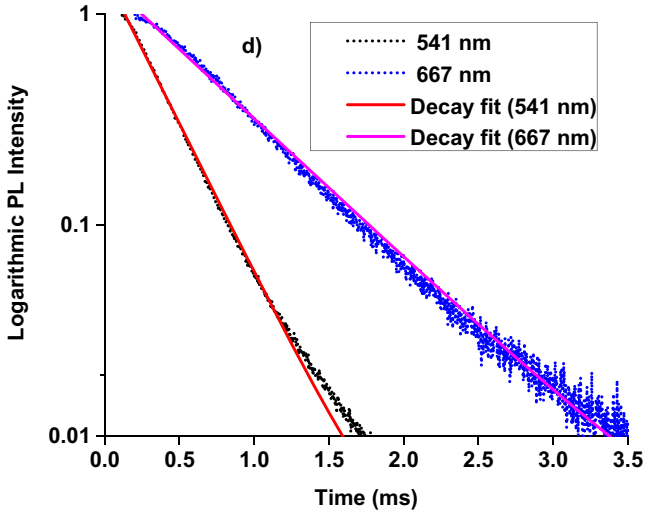

Fig. 8. a) Photograph of the as-prepared UCNP dispersion in a glass cuvette and b) UCNP dispersion under 976 nm laser excitation showing green luminescence, both at a UCNP dispersion concentration of 35 mg/mL. c) Luminescence spectra of the UCNP suspension recorded using a spectrofluorimeter (concentration of 3.5 mg/mL). d) Photoluminescence decay on a logarithmic scale with a linear fit (NP dispersion concentration of 3.5 mg/mL) showing a life time of $\tau = 324$ μs for the 541 nm emission peak and $\tau = 655$ μs for 667 nm emission peak.

section, Yb^{3+} ions absorb more photons from the laser exciting them from the $^2F_{7/2}$ to $^2F_{5/2}$ level and subsequently transferring the energy to Er^{3+} to excite them from $^4I_{15/2}$ level to the $^4I_{11/2}$ [1].

The cross-relaxation energy transfer process leads to an increased probability of photon absorption by the excited Er^{3+}: from the $^4I_{11/2}$ level to the $^4F_{7/2}$ level. As a result of non-radiative relaxation of Er^{3+} ions from $^4F_{7/2}$ to $^2H_{11/2}$ and $^4S_{3/2}$ and the subsequent radiative relaxation from these levels to $I_{15/2}$ results in green emission. Alternatively, the excited ion can relax non-radiatively from $^2H_{11/2}$ and $^4S_{3/2}$ levels and populate the $^4F_{9/2}$ level leading to red emission due to the $^4F_{9/2} \rightarrow {}^4I_{15/2}$ radiative transition. Regarding the red emission, the energy level Er^{3+}:$^4F_{9/2}$ can also be populated through two other processes, the efficiency of these are dependent on the host material and doping concentrations. The first one is excited state absorption from the $^4I_{13/2}$ level, which can be populated through non-radiative relaxation from the $^4I_{11/2}$ level. The second process is relaxation of $^4F_{7/2} \rightarrow {}^4F_{9/2}$ and $^4I_{11/2} \rightarrow {}^4F_{9/2}$ between two nearby Er^{3+} ions [40]. The green to red emission intensity ratio (G/R) was found to be 1.4 by consideration of the peak intensities at 539 nm and 667 nm for the excitation laser fluence used in this study. The photoluminescence decay lifetimes of the 541 nm and 667 nm emission of the UCNPs were obtained by linear fitting of the intensity in the logarithmic scale (Fig. 8d). From Fig. 8d, the $BaYF_5/Yb^{3+}/Er^{3+}$ particles studied in this paper have a photoluminescence lifetime values of $\tau = 324$ μs for 541 nm emission peak and $\tau = 655$ μs for 667 nm emission peak.

Photoluminescence imaging of the particles alone (*i.e.* following oven drying of a drop of UCNP suspension on a glass slide) showed green emission in accordance with the spectral results for the suspension (Fig. 9). During the process of drying the particles became aggregated and were monitored using the fluorescence microscope using 976 nm laser excitation.

In vitro X-ray μCT images of the UCNP suspensions at various nanoparticle concentrations are presented in Fig. 10 and these are quantified in terms of Hounsfield Units (HU) in Fig. 11. Hounsfield Units, which is a

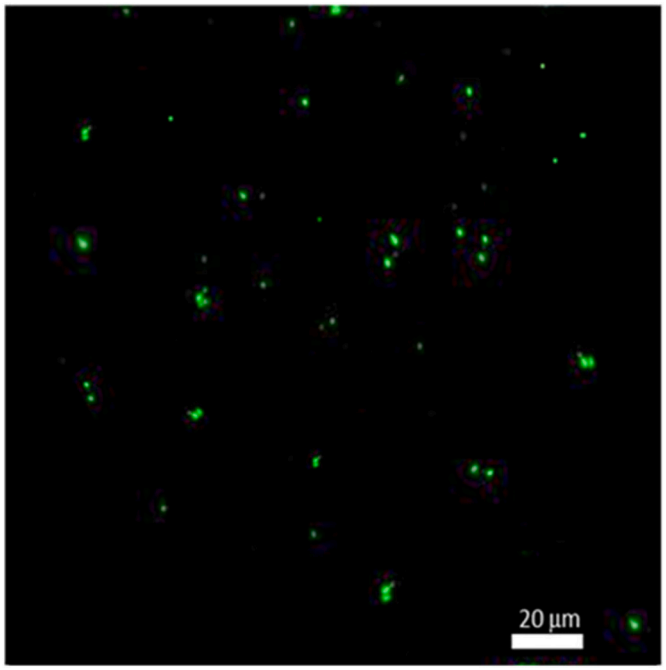

Fig. 9. Fluorescence micrograph while exciting a dried UCNP dispersion (concentration of 3.5 mg/mL) using a 976 nm laser.

relative quantitative measurement of radio density used by radiologists in the interpretation of computed tomography are commonly used for the quantification of contrast in both *in vitro* and *in vivo* X-ray µCT images [41,42]. The enhanced contrast associated with an increasing concentration of nanoparticles is evident in Fig. 10. However, a clear contrast was not observed for lower concentrations of particles (images of all the concentrations are not shown in Fig. 10), despite the HU value increasing for concentrations in the range 0.5 to 3.5 mg/mL (Fig. 11). However, at higher concentrations, the contrast is visibly prominent in the images shown in Fig. 10.

In comparison, the commercial X-ray imaging agent (iopromide injection solution) shows a value of <40 HU in the 0–3 mg/mL concentration range. The higher atomic number and density of Yb (70 and 6.8 g/cm^3) compared to iodine (53 and 4.9 g/cm^3) and also the increased atomic number and density of Ba contribute to the overall CT contrast of the UCNPs. We report an HU value of 123 for the current $BaYF_5/Yb^{3+}/Er^{3+}$ particles at a concentration level of 3.5 mg/mL, which is much higher when compared to various other rare earth-based systems previously studied, where a value of 140 is achieved only at a concentration

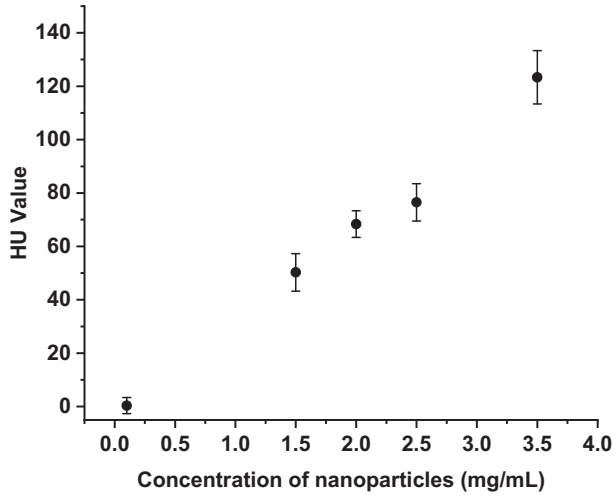

Fig. 11. Variation in Hounsfield unit (HU) values with concentration of UCNP dispersions.

of around 6.5 mg/mL [43]. The quantification of the contrast using HU values have not been undertaken in many studies even though certain *in vivo* imaging results have been previously reported using materials system similar to this material [25]. Thus results of the present study demonstrate good upconversion PL and X-ray µCT properties evident from the reported PL spectrum and Hounsfield Unit values for $BaYF_5/Yb^{3+}/Er^{3+}$ UCNPs. The sharpness of the red and green photoluminescence peaks will be advantageous for biosensing applications as well. The synergistic combination of upconversion PL properties and X-ray µCT contrast properties in a single nanoparticle system allows its application for dual mode imaging. As is well established, the phenomena of upconversion luminescence exhibited by the rare earth materials systems such as $BaYF_5/Yb^{3+}/Er^{3+}$ nanoparticles reported in this study produce minimal cell and tissue damage due to the 976 nm near infrared (NIR) excitation adopted. This is highly advantageous compared to the fluorescence exhibited by other nanoparticles, such as quantum dots and Au nanoparticles, which require UV excitation, resulting in limited tissue penetration and the possibility for phototoxicity, with damage to cells and tissues.

Future possible bioimaging applications of the material include improving the UCPL intensity by varying sensitizers-activator concentrations and combining with other modalities. Trimodal imaging combinations such as UCPL/CT/PET, by doping with PET isotopes such as ^{18}F, or UCPL/CT/MRI by doping with magnetic nuclei such as Gd^{3+} or Fe_3O_4 could be suitable candidates for more sensitive diagnostic imaging.

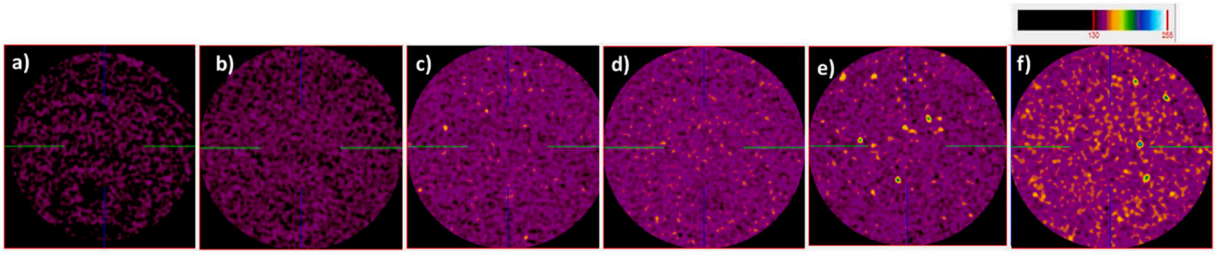

Fig. 10. The X-ray µCT images of samples with concentrations of $BaYF_5/Yb^{3+}/Er^{3+}$ UCNP samples: a) 0.1 mg/mL b) 1.5 mg/mL c) 2 mg/mL d) 2.5 mg/mL e) 3 mg/mL and f) 3.5 mg/mL.

4. Conclusions

Yb^{3+}/Er^{3+}-doped $BaYF_5$ upconversion nanoparticles were prepared with PEI using a hydrothermal route. Particles were found to be single crystalline with a cuboidal morphology and of a homogeneous chemical composition. TEM imaging revealed an average particle size of 47 ± 9 nm, whereas DLS showed a hydrodynamic size distribution peaked around 90 nm due to the presence of a hydrated PEI layer which provided good stability and dispersability in aqueous media, as well as better cell membrane permeability, as indicated by the high zeta potential value of +51 mV. The particles were non-toxic towards endothelial cells (90–100% cell viability) across a wide concentration range as established by an MTT assay. Excitation of a colloidal suspension of the particles at 976 nm wavelength indicated intense green photoluminescence with a less intense red peak. Fluorescence microscopy of the dried nanoparticles indicated high green emission, under excitation by a 976 nm laser. Quantification of X-ray μCT contrast images strongly confirmed the suitability of these materials as CT contrast agents. The synergistic combination of upconversion photoluminescence and X-ray μCT contrast properties in a single nanoparticle system allows dual mode imaging application. Future possibilities of these dual mode upconversion particles include trimodal imaging combinations for sensitive diagnostic imaging, incorporating magnetic nuclei and PET isotopes. Further investigations and detailed surface modifications with appropriate bioconjugation procedures on these particles could be adopted for using these particles in biosensing of disease markers and bioimaging applications.

CRediT authorship contribution statement

Corresponding author, Padmaja Parameswaran Nampi: Conceptualization, Experimental executions and characterisation, Original manuscript preparation, Fellowship. **Alexander Vakurov**: Experimental, Software. **Hema Viswambharan**: Data acquisition (cell toxicity) and discussion. **Jürgen E. Schneider**: Validation of CT results. **Rik Brydson**: Data supervision and suggestion on detailed structural characterisation, Reviewing. **Paul A. Millner**: Experimental facilities, resources and Reviewing. **Sikha Saha**: Supervision on dealing with biological prospects. **Gin Jose**: Supervision, Reviewing, Funding.

Declaration of competing interest

The authors declare that they have no known competing financial interests or personal relationships that could have appeared to influence the work reported in this paper.

Acknowledgments

The corresponding author, Padmaja Parameswaran Nampi (PPN) received funding from the H2020 Marie Skłodowska-Curie Actions, European Union under the Grant Agreement No. RECORDER-707297 to carry out this work. Alexander Vakurov was funded by the Natural Environment Research Council, United Kingdom (Grant No. NE/N007581/1). The authors also would like to thank EPSRC, United Kingdom for the financial support through the research grants (EP/M015165/1 and EP/T004711/1). Jürgen E. Schneider (JES) acknowledges funding from the British Heart Foundation (Grant No. SI/14/1/30718). PPN expresses her gratitude to Zabeada Aslam, Faith Bamiduro, Eric Kumi Barimah, Tarun Kakkar and Joanna Koch for their support with transmission electron microscopy, XRD, fluorescence lifetime, fluorescence microscopy and X-ray μCT measurements respectively.

Appendix A. Supplementary data

Supplementary data to this article can be found online at https://doi.org/10.1016/j.msec.2021.111937.

References

[1] F. Auzel, Upconversion and anti-Stokes processes with f and d ions in solids, Chem. Rev. 104 (2003) 139–174.
[2] F. Wang, X. Liu, Recent advances in the chemistry of lanthanide-doped upconversion nanocrystals, Chem. Soc. Rev. 38 (2009) 976–989.
[3] J.C. Zhou, Z.L. Yang, W. Dong, R.J. Tang, L.D. Sun, C.H. Yan, Bioimaging and toxicity assessments of near-infrared upconversion luminescent $NaYF_4$:Yb, Tm nanocrystals, Biomaterials 32 (2011) 9059–9067.
[4] L. Xiong, T. Yang, Y. Yang, C. Xu, F. Li, Long- term in vivo biodistribution imaging and toxicity of polyacrylic acid-coated upconversion nanophosphors, Biomaterials 31 (2010) 7078–7085.
[5] J. Zhou, Z. Liu, F. Li, Upconversion nanophosphors for small-animal imaging, Chem. Soc. Rev. 41 (2012) 1323–1349.
[6] M. Haase, H. Schäfer, Upconverting nanoparticles, Angew. Chem. Int. Ed. 50 (2011) 5808–5829.
[7] F. Wang, Y. Han, C.S. Lim, Y.H. Lu, J. Wang, J. Xu, H.Y. Chen, C. Zhang, M. H. Hong, X. Liu, Simultaneous phase and size control of upconversion nanocrystals through lanthanide doping, Nature 463 (2010) 1061–1065.
[8] M. Nyk, R. Kumar, T.Y. Ohulchanskyy, E.J. Bergey, P.N. Prasad, High contrast in vitro and in vivo photoluminescence bioimaging using near infrared to near infrared up-conversion in Tm^{3+} and Yb^{3+} doped fluoride nanophosphors, Nano Lett. 8 (2008) 3834–3838.
[9] H. Guo, Z. Li, H. Qian, Y. Hu and I.N. Muhammad, Seed-mediated synthesis of $NaYF_4$:Yb, Er/$NaGdF_4$ nanocrystals with improved upconversion fluorescence and MR relaxivity, Nanotechnology 21 (2010) 125602.
[10] H. Shen, F. Wang, X. Fan, M. Wang Synthesis of LaF_3:Yb^{3+},Ln^{3+} nanoparticles with improved upconversion luminescence, J. Exp. Nanosci. 2:4 (2007) 303–311.
[11] J.C. Boyer, L.A. Cuccia, J.A. Capobianco, Synthesis of colloidal upconverting $NaYF_4$:Er^{3+}/Yb^{3+} and Tm^{3+}/Yb^{3+}monodisperse nanocrystals, Nano Lett. 7 (2007) 847–852.
[12] F. Wang, X. Liu, Upconversion multicolor fine-tuning: visible to near-infrared emission from lanthanide-doped $NaYF_4$ nanoparticles, J. Am. Chem. Soc. 130 (2008) 5642–5643.
[13] H. Mai, Y. Zhang, R. Si, Z. Yan, L. Sun, L. You, C. Yan, High-quality sodium rare-earth fluoride nanocrystals: controlled synthesis and optical properties, J. Am. Chem. Soc. 128 (2006) 6426–6436.
[14] D. Chen, Y. Yu, F. Huang, A. Yang, Y. Wang, Modifying the size and shape of monodispersed bifunctional alkaline-earth fluoride nanocrystals through lanthanide doping, J. Am. Chem. Soc. 132 (2010) 9976–9978.
[15] X. Qiao, X. Fan, M. Wang, H. Yang, and X. Zhang, Luminescence behavior of Er^{3+}doped glass ceramics containing Sr_2RF_7 (R=Y,Gd,La) nanocrystals, J. Appl. Phys. Lett. 104 (2008) 043508.
[16] S.L. Zhao, S.Q. Xu, D.G. Deng, H.P. Wang, L.H. Huang, X.P. Fan, Spectroscopic properties Eu^{3+} doped and Tm^{3+}/Yb^{3+} codoped oxyfluoride glass ceramics containing Ba_2GdF_7 nanocrystals, Chem. Phys. Lett. 494 (2010) 202–205.
[17] Y. Bu, S. Xiao, X. Wang, W. Yuan, J.W. Ding, Preparation and upconversion properties of Ba_2ErF_7 and Ba_2ErF_7:Yb^{3+} powders, J. Lumin. 130 (2010) 38–44.
[18] F. Vetrone, V. Mahalingam, J.A. Capobianco, Near-infrared-to-blue upconversion in colloidal $BaYF_5$:Tm^{3+}, Yb^{3+}nanocrystals, Chem. Mater. 21 (2009) 1847–1851.
[19] Y. Huang, H. You, G. Jia, Y. Song, Y. Zheng, M. Yang, K. Liu, N. Guo, Hydrothermal synthesis, cubic structure, and luminescence properties of $BaYF_5$:RE (RE = Eu, Ce, Tb) nanocrystals, J. Phys. Chem. C (2010) 18051–18058, 114.
[20] C. Zhang, P. Ma, C. Li, G. Li, S. Huang, D. Yang, M. Shang, X. Kang, J. Lin, Controllable and white upconversion luminescence in $BaYF_5$:Ln^{3+} (Ln = Yb, Er, Tm) nanocrystals, J. Mater. Chem. 21 (2011) 717–723.
[21] H.J. Guggenheim, L.F. Johnson, New fluoride compounds for efficient infrared-visble conversion, Appl. Phys. Lett. 15 (1969) 51–52.
[22] F. Liu, Y.S. Wang, D.Q. Chen, Y.L. Yu, E. Ma, L.H. Zhou, Upconversion emission of a novel glass ceramic containing Er^{3+}:$BaYF_5$ nanocrystals, Mater. Lett. 61 (2007) 5022–5025.
[23] G.S. Yi, W.B. Lee, G.M. Chow, Synthesis of $LiYF_4$, $BaYF_5$, and $NaLaF_4$ optical nanocrystals, J. Nanosci. Nanotechnol. 7 (2007) 2790–2794.
[24] H.L. Qiu, G.Y. Chen, L. Sun, S.W. Hao, G. Han, C.H. Yang, Ethylenediaminetetraacetic acid (EDTA)-controlled synthesis of multicolour lanthanide doped $BaYF_5$ upconversion nanocrystals, J. Mater. Chem. 21 (2011) 17202–17208.
[25] H. Liu, W. Lu, H. Wang, L. Rao, Z. Yi, S. Zeng, J. Hao, Simultaneous synthesis and amine-functionalization of single-phase $BaYF_5$:Yb/Er nanoprobe for dual-modal in vivo upconversion fluorescence and long-lasting X-ray computed tomography imaging, Nanoscale 5 (2013) 6023–6029.
[26] M. Kraft, C. Würth, V. Muhr, T. Hirsch, U. Resch-Genger, Particle-size-dependent upconversion luminescence of $NaYF_4$:Yb, Er nanoparticles in organic solvents and water at different excitation power densities, Nano Res.11 (2018) 6360–6374.
[27] Y. Shang, S. Hao, J. Liu, M. Tan, N. Wang, C. Yang, G. Chen, Synthesis of Upconversion β-$NaYF_4$:$Nd^{3+}/Yb^{3+}/Er^{3+}$ particles with enhanced luminescent intensity through control of morphology and phase, Nanomaterials (Basel). 5 (1) (2015) 218–232.
[28] J. Xu, A. Gulzar, P. Yang, H. Bi, D. Yang, S. Gai, F. He, J. Lin, B. Xing, D. Jin, Recent advances in near-infrared emitting lanthanide-doped nanoconstructs: mechanism, design and application for bioimaging, Coord, Chem.Rev. 381 (2019) 104–134.
[29] S. Dong, J. Xu, T. Jia, M. Xu, C. Zhong, G. Yang, J. Li, D. Yang, F. He, S. Gai, P. Yang, J. Lin, Upconversion-mediated $ZnFe_2O_4$ nanoplatform for NIR-enhanced chemodynamic and photodynamic therapy, Chem. Sci. 10 (2019) 4259–4271.
[30] H. Li, R. Wei, G. –H. Yan, J. Sun, C. Li, H. Wang, L. Shi, John A. Capobianco and L. Sun, Smart self-assembled nanosystem based on water-soluble pillararene and rare-

earth-doped upconversion nanoparticles for pH-responsive drug delivery ACS Appl. Mater. Interfaces 10 (2018) 4910–4920.
[31] S. Zhang, J. Wang, W. Xu, B.T. Chen, W. Yu, L. Xu, H.W. Song, Fluorescence resonance energy transfer between $NaYF_4$:Yb,Tm upconversion nanoparticles and gold nanorods: near-infrared responsive biosensor for streptavidin, J. Lumin. 147 (2014) 278–283.
[32] P.P. Nampi, A. Vakurov, L.E. Mackenzie, N.S. Scrutton, P.A. Millner, G. Jose, S. Saha, Selective cellular imaging with lanthanide-based upconversion nanoparticles, J. Biophotonics 12 (2019), e201800256.
[33] M. Gunaseelan, S. Yamini, G.A. Kumar, C. Santhosh, J. Senthilselvan, Photon upconversion characteristics of intense green emitting $BaYF_5$:Yb^{3+}, Er^{3+} nanoclusters prepared by reverse microemulsion, Mater. Res. Bull. 107 (2018) 366–378.
[34] R. Sang, Y. Li, X. Ma, Z. Cui, Y. Liu, Synthesis and optical properties of erbium-doped BaF_2 nanoparticles, Mater. Chem. Phys. 143 (2014) 1315–1318.
[35] David B. Williams, C. Barry Carter, Transmission Electron Microscopy-A Textbook for Materials Science, Springer, 2009.
[36] J.K. Lim, S.P. Yeap, H.X. Che, S.C. Low, Characterization of magnetic nanoparticle by dynamic light scattering, Nanoscale Res. Lett. 8 (1) (2013) 381.
[37] O.S. Wolfbeis, An overview of nanoparticles commonly used in fluorescent bioimaging, Chem. Soc. Rev. 44 (2015) 4743–4768.
[38] J. Sun, J. Xian, X. Zhang, H. Du, Size and shape controllable synthesis of oil-dispersible $BaYF_5$: Yb^{3+}/Er^{3+} upconversion fluorescent nanocrystals, J. Alloys Compd. 509 (2011) 2348–2354.
[39] J. Sun, J. Xian, X. Zhang, H. Du, Synthesis of well oil-dispersible $BaYF_5$:Yb^{3+}/Er^{3+} nanocrystals with green upconversion fluorescence, J. Rare Earths 28 (2010) 219–221.
[40] J. Zhao, J. Wu, J. Xue, Q. Zhu, W. Ni, Au/$NaYF_4$:Yb,Er binary superparticles: synthesis and optical properties, Isr. J. Chem. 56 (2016) 242–248.
[41] H. Lusic, M.W. Grinstaff, X-ray computed tomography contrast agents, Chem. Rev. 113 (2013), https://doi.org/10.1021/cr200358s.
[42] C. A. Wathen, N. Foje, T. van Avermaete, B. Miramontes, S. E. Chapman, T. A. Sasser, R. Kannan, S. Gerstler and W. M. Leevy, In vivo X-ray computed tomographic imaging of soft tissue with native, intravenous, or oral contrast, Sensors (Basel) 13 (2013) 6957–980; https://doi.org/10.3390/s130606957.
[43] Y. Sun, X. Zhu, J. Peng, F. Li, Core–shell lanthanide upconversion nanophosphors as four-modal probes for tumor angiogenesis imaging, ACS Nano l7 (2013) 11290–11300.